

Article

Quantum-Mechanical Study of Nanocomposites with Low and Ultra-Low Interface Energies

Martin Friák ^{1,*} , David Holec ²  and Mojmír Šob ^{3,1,4}

¹ Institute of Physics of Materials, Academy of Sciences of the Czech Republic, Žižkova 22, CZ-616 62 Brno, Czech Republic; mojmir@ipm.cz

² Department of Materials Science, Montanuniversität Leoben, Franz-Josef-Strasse 18, A-8700 Leoben, Austria; david.holec@unileoben.ac.at

³ Department of Chemistry, Faculty of Science, Masaryk University, Kotlářská 2, CZ-611 37 Brno, Czech Republic

⁴ Central European Institute of Technology, CEITEC MU, Masaryk University, Kamenice 5, CZ-625 00 Brno, Czech Republic

* Correspondence: friak@ipm.cz; Tel.: +420-532-290-400

Received: 27 November 2018; Accepted: 12 December 2018; Published: 15 December 2018

Abstract: We applied first-principles electronic structure calculations to study structural, thermodynamic and elastic properties of nanocomposites exhibiting nearly perfect match of constituting phases. In particular, two combinations of transition-metal disilicides and one pair of magnetic phases containing the Fe and Al atoms with different atomic ordering were considered. Regarding the disilicides, nanocomposites MoSi₂/WSi₂ with constituents crystallizing in the tetragonal C11_b structure and TaSi₂/NbSi₂ with individual phases crystallizing in the hexagonal C40 structure were simulated. Constituents within each pair of materials exhibit very similar structural and elastic properties and for their nanocomposites we obtained ultra-low (nearly zero) interface energy (within the error bar of our calculations, i.e., about 0.005 J/m²). The interface energy was found to be nearly independent on the width of individual constituents within the nanocomposites and/or crystallographic orientation of the interfaces. As far as the nanocomposites containing Fe and Al were concerned, we simulated coherent superlattices formed by an ordered Fe₃Al intermetallic compound and a disordered Fe-Al phase with 18.75 at.% Al, the α -phase. Both phases were structurally and elastically quite similar but the disordered α -phase lacked a long-range periodicity. To determine the interface energy in these nanocomposites, we simulated seven different distributions of atoms in the α -phase interfacing the Fe₃Al intermetallic compound. The resulting interface energies ranged from ultra low to low values, i.e., from 0.005 to 0.139 J/m². The impact of atomic distribution on the elastic properties was found insignificant but local magnetic moments of the iron atoms depend sensitively on the type and distribution of surrounding atoms.

Keywords: MoSi₂; WSi₂; TaSi₂; NbSi₂; elasticity; ab initio; interface energies; Fe₃Al; disorder

1. Introduction

Ever increasing demand for energy-conversion units exhibiting a higher efficiency leads to increasing operating temperatures in these systems and, therefore, new materials, which would sustain such conditions, are needed. Because the development of these materials is highly complex and multi-faceted, combinations of often mutually-conflicting properties are rarely found in a single-phase structures. Composites then represent a critically important class of materials. In particular, coherent nanocomposites require optimum matching of constituting phases for their stability and rather low interface energies. In our study, we addressed three nanocomposites combining materials intended for high or elevated temperature applications: two pairs of transition-metal disilicides that are predicted

to possess ultra-low interface energies and then a pair of two different phases from the Fe-Al system, which are expected to have the interface energies ranging from ultra low to low values.

Regarding the transition-metal silicides, they are currently considered as very promising bases for future high-temperature structural materials (see, e.g., Refs. [1–4]), in particular for operational temperatures above those of Ni-based superalloys. At high temperatures, transition-metal silicides are known to combine the ductility and thermal conductivity of metals with high strength and corrosion resistance of ceramics. As far as composites combining them are concerned, MoSi₂/WSi₂ composite powders with different phase compositions are fabricated via a self-propagating high-temperature synthesis (SHS) method [5]. This approach is widely recognized as an effective manufacturing strategy for the fabrication of materials applied in high-temperature fields, in particular for refractories such as transition-metal carbides, nitrides, silicides, and borides [6]. Preparation of MoSi₂/WSi₂ composites using elemental powders of Mo, W and Si by the thermal explosion mode of SHS have been theoretically calculated and investigated by experiments in Ref. [7]. Phase composition and microchemical area analyses were conducted by XRD, SEM and EDAX methods. Pure MoSi₂/WSi₂ composites are fabricated by the thermal explosion mode of SHS, and MoSi₂/WSi₂ exists as a solid solution of (Mo_xW_{1-x})Si₂ but the chemical elements inside of individual grains are not uniformly distributed. As an alternative processing route, five kinds of WSi₂/MoSi₂ composites are fabricated by mechanical alloying in [8]. WSi₂-reinforced MoSi₂ composites are successfully prepared also by mechanical activation followed by in situ reactive spark plasma sintering of Mo, Si, and W elemental powders in [9]. The addition of W to the reactants leads to a finer microstructure than that obtained using pure MoSi₂, resulting in a significant improvement of mechanical properties. The Vicker's hardness of 20 vol % WSi₂/MoSi₂ is as high as 16.47 GPa. Nanocomposite of (Mo,W)Si₂/WSi₂ was synthesized via mechanical alloying (MA) and heat treatment in Ref. [10]. Increasing the milling time to 80 h followed by the post-annealing at 1000 °C caused the complete formation of (Mo,W)Si₂/WSi₂ nanocomposite. MoSi₂/WSi₂ composites were successfully prepared by pressureless sintering from mechanically-assisted combustion synthesized powders in [11].

Motivated by the above-mentioned studies of MoSi₂/WSi₂ (nano)composites containing structurally and elastically very similar pair of materials crystallizing in the C11_b structure, we also assessed another pair of matching materials, TaSi₂ and NbSi₂, which are crystallizing in the C40 structure.

Finally, as a system with rather low interface energy, we studied nanocomposites formed by two phases from the Fe-Al binary system [12–15]. These materials are also considered as promising for elevated-temperature applications and as such they are intensively studied [16–40]. A sub-class of Fe-Al-based materials is represented by composites consisting of an ordered Fe₃Al with the D0₃ structure and a disordered Fe-Al solid solution with about 18–19 at.% Al. The existence of these composites can be experimentally proved using, for example, Mössbauer spectroscopy [41] or transmission electron microscopy (TEM) techniques. The latter are sensitive to anti-phase boundaries (APBs), which have a different character in Fe₃Al and the Fe-Al phase [42–45].

2. Methods

Our quantum-mechanical calculations were performed within the framework of density functional theory [46,47] using the Vienna Ab initio Simulation Package (VASP) [48,49] and projector augmented wave (PAW) pseudopotentials [50,51]. When studying the transition-metal disilicides, the exchange and correlation energy was treated in the local density approximation (LDA) [52] but, in the case of phases containing the Fe and Al atoms, the generalized gradient approximation (GGA) parameterized by Perdew and Wang [53] (PW91) with the Vosko–Wilk–Nusair correction [54] was necessary to correctly reproduce the ground-state D0₃ structure of Fe₃Al. Regarding the MoSi₂ and WSi₂, we used a plane-wave energy cut-off of 400 eV and the k-point Monkhorst–Pack [55] meshes contained 20 × 20 × 2 (10 × 10 × 8) k-points in the case of 24-atom supercells modeling the superlattices with stacking along the [001] ([100] and [110]) directions. The calculations for TaSi₂ and NbSi₂ required the

cut-off energy of 480 eV and the $12 \times 12 \times 4$ k-point mesh in the case of 18-atom supercells. When computing Fe-Al-based nanocomposites, the cut-off energy was equal to 350 eV and the sampling of the Brillouin zone was done using Monkhorst–Pack grids with $10 \times 10 \times 6$ k-points in the case of computational supercells containing 32 atoms. All calculations had an estimated error-bar of about 0.001 eV/atom. Finally, the second-order elastic constants were determined using the stress-strain method [56].

3. Results

The first type of studied nanocomposite containing transition-metal disilicides is visualized in Figure 1a. WSi_2 and MoSi_2 , which crystallize in the tetragonal C11_b structure, form a coherent nanocomposite where two conventional cells of each materials are stacked one on top of the other along the [001] direction (the interfaces are perpendicular to this direction) and alternate. It should be emphasized that, due to the periodic boundary conditions, which are applied to all nanocomposites in our calculations, the simulated nanocomposites form so-called superlattices [57–78] when the atomic planes continue from one phase into another.

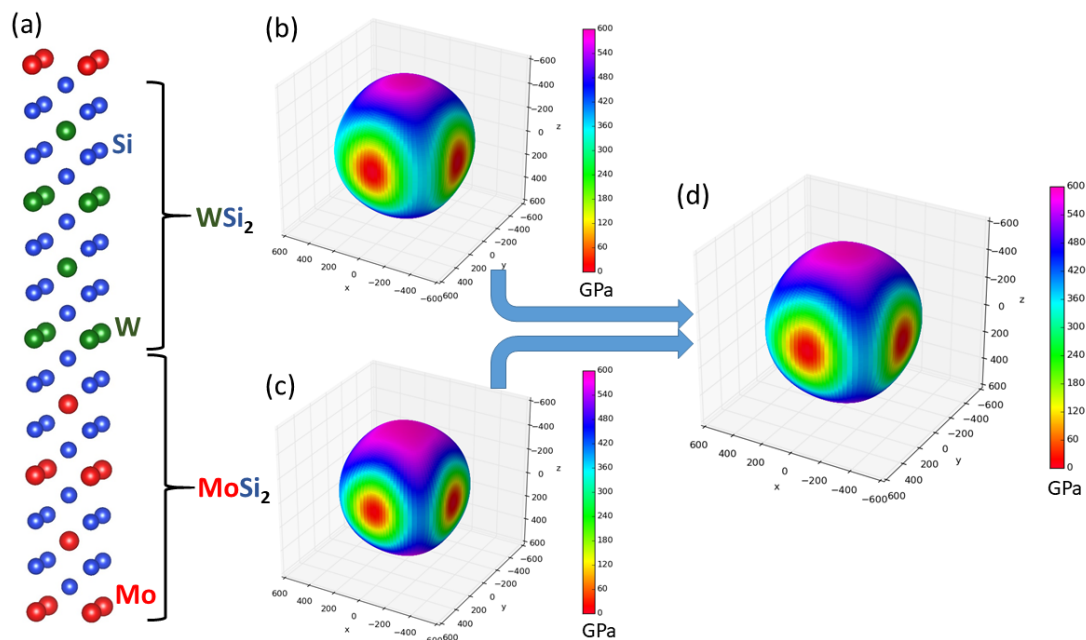


Figure 1. Visualization of a $\text{WSi}_2/\text{MoSi}_2$ nanocomposite (a superlattice) with the stacking along (and the interfaces perpendicular to) the [001] direction within the C11_b lattice (a) accompanied with directional dependences of the Young's modulus of bulk WSi_2 (b), bulk MoSi_2 (c) and the composite $\text{WSi}_2/\text{MoSi}_2$ (d) formed out of them. The parts (b–d) were visualized by the SC-EMA [79–81] library (scema.mpie.de) based on ab initio computed elastic constants.

As seen in Table 1, both disilicides have very similar lattice parameters a and c describing their tetragonal structure and also quite similar elastic properties. Our theoretical values are in excellent agreement with both experimental data and previous calculations. The elasticity of bulk phases is conveniently visualized in Figure 1b,c in the form of directional dependences of the Young's modulus. The values for this composite with an equal amount of both phases are listed in Table 1 at the line for the composition $(\text{WSi}_2)_4(\text{MoSi}_2)_4$.

Table 1. Calculated structural characteristics and elastic constants of bulk MoSi₂ and WSi₂ as well as of their composite MoSi₂/WSi₂ with the stacking along (and the interfaces perpendicular to) the [001] direction within the C11_b lattice. The computed values are complemented by experimental data from the literature. As far as the lattice parameters *a* and *c* of the C11_b structure are concerned, the values for the *c* lattice parameters of the nanocomposites are marked by the symbol of an asterisk * because they are divided by a factor of 4 to be compared with the values for the bulk unit cells of the individual constituents (bulk MoSi₂ and WSi₂). The simulated nanocomposites are shown in Figure 2 and, specifically for the equal amount of both phases, in Figure 1a. Experimental elastic constants of MoSi₂ and WSi₂ were taken from Refs. [82,83].

Composition	<i>a</i> (Å)	<i>c</i> (Å)	C ₁₁ (GPa)	C ₁₂ (GPa)	C ₁₃ (GPa)	C ₃₃ (GPa)	C ₄₄ (GPa)	C ₆₆ (GPa)
MoSi ₂	3.176	7.781	428	125	101	537	208	207
	3.202 [83]	7.855 [83]	417.0 [82]	104.2 [82]	83.8 [82]	514.5 [82]	204.2 [82]	193.6 [82]
(WSi ₂) ₁ /(MoSi ₂) ₇	3.178	7.782 *	433	126	101	542	210	209
(WSi ₂) ₂ /(MoSi ₂) ₆	3.180	7.781 *	437	127	102	546	210	210
(WSi ₂) ₃ /(MoSi ₂) ₅	3.181	7.781 *	440	127	102	551	211	212
(WSi ₂) ₄ /(MoSi ₂) ₄	3.183	7.780 *	444	127	103	555	212	213
(WSi ₂) ₅ /(MoSi ₂) ₃	3.185	7.780 *	447	127	103	560	212	214
(WSi ₂) ₆ /(MoSi ₂) ₂	3.186	7.780 *	450	128	106	565	213	216
(WSi ₂) ₇ /(MoSi ₂) ₁	3.188	7.780 *	453	128	106	570	213	217
WSi ₂	3.188	7.778	456	131	105	576	214	217
	3.211 [83]	7.835 [83]	442.8 [82]	121.7 [82]	81.0 [82]	552.3 [82]	211.6 [82]	217.5 [82]

As a consequence of the similarity of the elastic constants of both constituents, the overall elastic properties of their nanocomposites are quite similar, too.

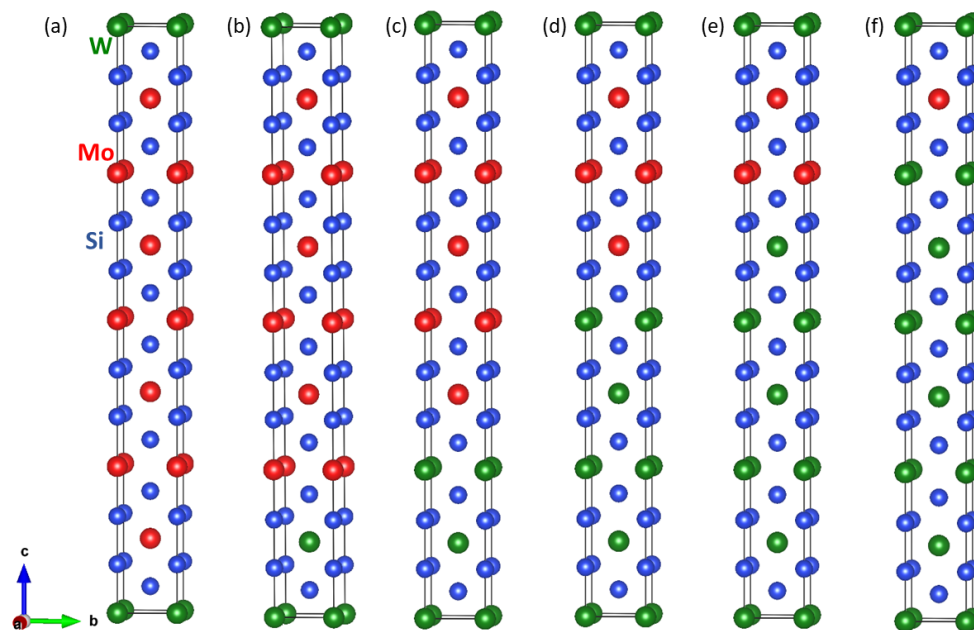


Figure 2. Schematic visualization of supercells modeling various nanocomposites with the stacking along (and the interfaces perpendicular to) the [001] direction. The mutual ratio of the constituents varies from 1:7, i.e., $(\text{WSi}_2)_1(\text{MoSi}_2)_7$, in the case of sub-figure (a), via 2:6 (b) and 3:5 (c) further for the opposite ratios 5:3 (d) and 6:2 (e) to 7:1, i.e., $(\text{WSi}_2)_7(\text{MoSi}_2)_1$, in the case of sub-figure (f).

Next, we evaluated the interface energy of the nanocomposites according to the formula:

$$\gamma((\text{WSi}_2)_m/(\text{MoSi}_2)_n) = \frac{E((\text{WSi}_2)_m/(\text{MoSi}_2)_n) - m \cdot E(\text{WSi}_2) - n \cdot E(\text{MoSi}_2)}{(2 \cdot A)} \quad (1)$$

using the energy $E((\text{WSi}_2)_m/(\text{MoSi}_2)_n)$ of the supercell modeling the nanocomposite $(\text{WSi}_2)_m/(\text{MoSi}_2)_n$, which contains m formula units of WSi_2 and n formula units of MoSi_2 , the energies of bulk phases of each constituent $E(\text{WSi}_2)$ and $E(\text{MoSi}_2)$ and the area of the interface A . Importantly, very probably due to the similarity of both constituents, the interface energy was found to be ultra low, essentially zero within the error bar of our calculations, i.e., the energy differences in Equation (1) are smaller than 0.001 eV/atom and the interface energies are then smaller than about 0.005 J/m².

To examine how the ultra-low interface energies depend on the width of the layers containing individual constituents within the nanocomposite as well as on the ratio of amount of both materials, we simulated a series of seven other superlattices with varying width of the constituents, as visualized in Figure 2. The calculated structural and elastic parameters are summarized in Table 1. The lattice parameter a increased quite monotonously from the value calculated for bulk MoSi_2 to that obtained for bulk WSi_2 . The changes of the lattice parameter c are much smaller because the values found for bulk MoSi_2 and WSi_2 are only very slightly different. Rather monotonous changes appear also for the elastic constants with all of them increasing when increasing the amount of elastically stiffer WSi_2 . Importantly, all the studied nanocomposites have again ultra low interface energies, which are essentially zero within the error-bar of our calculations. Next, as seen in the Appendix, the ultra low interface energies were nearly independent of the crystallographic orientation of the interface.

After examining the $\text{WSi}_2/\text{MoSi}_2$ nanocomposites, which were experimentally reported to exist, we next drew our attention to another class of nanocomposites containing transition-metal disilicides, which were structurally and elastically very similar. The studied TaSi_2 and NbSi_2 crystallize in the hexagonal C40 structure and, therefore, we simulated a superlattice based on this structure (see Figure 3).

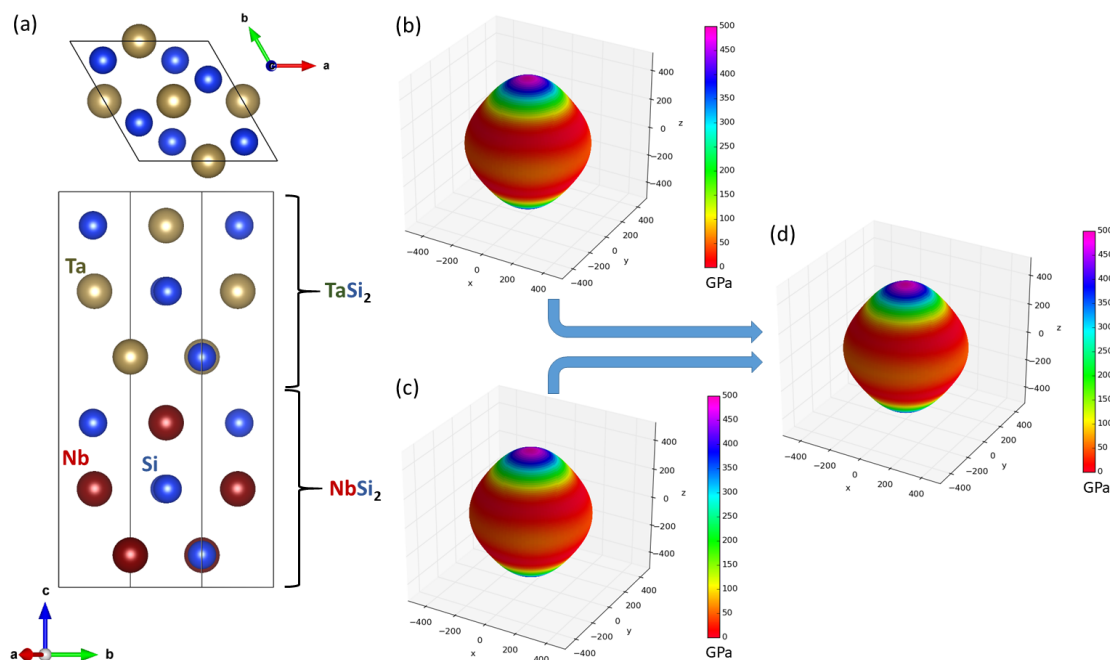


Figure 3. A top-view and a side-view of the computational supercell used in our calculations as a model of $\text{TaSi}_2/\text{NbSi}_2$ nanocomposite (a superlattice) with the stacking along (and the interfaces perpendicular to) the $[0001]$ direction within the C40 lattice (a) accompanied with directional dependences of the Young's modulus of bulk TaSi_2 (b), bulk NbSi_2 (c) and their composite $\text{TaSi}_2/\text{NbSi}_2$ (d).

The nanocomposites have the interfaces perpendicular to the $[0001]$ crystallographic direction. The lattice parameters a and c and elastic constants of both constituents in their bulk phases are summarized in Table 2. Our theoretical values are in an excellent agreement with both experimental data and previous calculations. Both disilicides have all the parameters very similar. The elasticity of bulk phases is conveniently visualized in Figure 3b,c in the form of directional dependences of the Young's modulus. As the elastic properties are quite similar, the elasticity of the studied nanocomposite is not too different from that of the constituting phases (see Figure 3d). Importantly, the interface energy is ultra low for this superlattice, again zero within the error-bar of our calculations.

Similar to the case of the $\text{WSi}_2/\text{MoSi}_2$ nanocomposites studied above, we examined how the ultra-low interface energies depend on the molar ratio of the constituting phases as well as on the width of the phases forming the superlattice (see Figure 4). We performed our calculations for a series of six other nanocomposites with different ratio of the TaSi_2 and NbSi_2 (see Figure 4a–f). Out of the six calculated superlattices shown in Figure 4, those shown in Figure 4c,d have the same ratio of the amount of both materials but a higher number of internal interfaces, six and four, respectively.

When evaluating the interface energies, they were again found to be ultra low, namely zero within the error-bar of our calculations. The lattice parameters a and c of the C40-based structure are concerned were rather monotonously increasing from their lower values in TaSi_2 to higher values in NbSi_2 . In contrast to this trend, the elastic constants rather monotonously decreased from their higher values in TaSi_2 to lower values in NbSi_2 .

Table 2. Calculated structural characteristics and elastic constants of bulk TaSi₂ and NbSi₂ as well as of their nanocomposites TaSi₂/NbSi₂ with the stacking along (and the interfaces perpendicular to) the [0001] direction within the C40 lattice. The computed values are complemented by both experimental data as well as by other theoretical results from literature. As far as the lattice parameters *a* and *c* of the C40 structure are concerned, the values of the lattice parameter *c* for the nanocomposites are marked by an asterisk * because they are divided by factor of 2 to be compared with the values for the bulk unit cells of the individual constituents (bulk TaSi₂ and NbSi₂). Experimental elastic constants of TaSi₂ and NbSi₂ were taken from Ref. [84] and theoretical ones from Refs. [85,86].

Composition	<i>a</i> (Å)	<i>c</i> (Å)	C ₁₁ (GPa)	C ₁₂ (GPa)	C ₁₃ (GPa)	C ₃₃ (GPa)	C ₄₄ (GPa)
TaSi ₂	4.736	6.530	394	85	101	487	143
	4.77 [84]	6.55 [84]	375.3 [84]	78.4 [84]	90.1 [84]	467.7 [84]	143.7 [84]
	4.731 [85]	6.501 [85]	392.2 [85]	78.3 [85]	98.2 [85]	484.6 [85]	148.8 [85]
	–	–	351.0 [86]	84.0 [86]	73.0 [86]	461.0 [86]	123.0 [86]
(NbSi ₂) ₁ /(TaSi ₂) ₅ —Figure 4a	4.739	6.534 *	392	84	99	483	143
(NbSi ₂) ₂ /(TaSi ₂) ₄ —Figure 4b	4.742	6.539 *	390	83	98	479	142
(NbSi ₂) ₃ /(TaSi ₂) ₃ —Figure 3a	4.745	6.543 *	387	82	96	475	142
(NbSi ₂) ₃ /(TaSi ₂) ₃ —Figure 4c	4.745	6.543 *	387	82	96	476	142
(NbSi ₂) ₃ /(TaSi ₂) ₃ —Figure 4d	4.745	6.543 *	388	82	96	476	142
(NbSi ₂) ₄ /(TaSi ₂) ₂ —Figure 4e	4.748	6.547 *	385	81	95	472	142
(NbSi ₂) ₅ /(TaSi ₂) ₁ —Figure 4f	4.751	6.551 *	383	80	94	469	141
NbSi ₂	4.754	6.555	380	79	92	465	141
	4.79 [84]	6.59 [84]	380.2 [84]	75.9 [84]	88.3 [84]	468.0 [84]	145.3 [84]
	4.747 [85]	6.529 [85]	378.9 [85]	73.0 [85]	90.2 [85]	462.5 [85]	144.6 [85]
	–	–	344.0 [86]	85.0 [86]	69.0 [86]	456.0 [86]	115.0 [86]

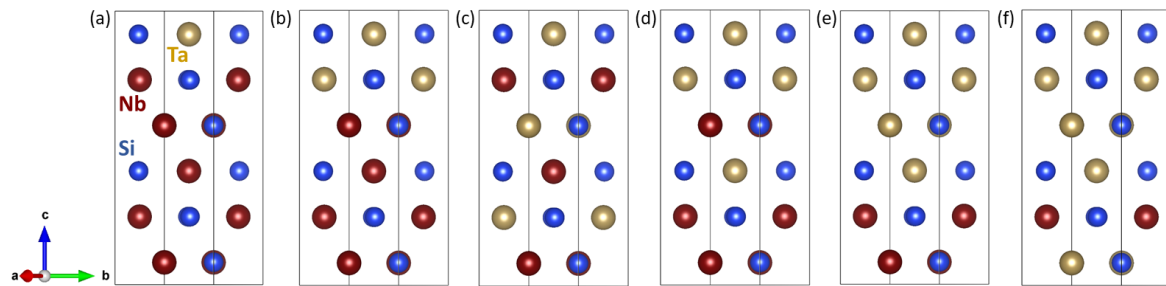


Figure 4. Schematic visualization of simulated $\text{NbSi}_2/\text{TaSi}_2$ nanocomposites with the stacking along (and the interfaces perpendicular to) the $[0001]$ direction. The mutual ratio of the amount of constituents varies from 1:5, i.e., $(\text{NbSi}_2)_1(\text{TaSi}_2)_5$ in the case of (a) via 2:4 (b), 3:3 (c,d) to 4:2 (e) and 5:1, i.e., $(\text{NbSi}_2)_5(\text{TaSi}_2)_1$ in the case of (f). Variants shown in (c,d) have an equal amount of both constituting phases (similar to the case of Figure 3a) but a different arrangement of atomic layers. Consequently, there is a higher number of internal interfaces (6 and 4 in the case of (c,d), respectively) and the layers with different constituents have different widths.

The last systems studied here is that containing two different phases from the binary iron-aluminium system, in particular, an ordered Fe_3Al intermetallic compound crystallizing in the $D0_3$ structure and a disordered solid solution of 18.75 at.% of Al with a body-centered cubic (bcc) ferromagnetic (FM) matrix, so-called α - or B2 phase. The structure of the former was derived from the bcc lattice and, therefore, both materials structurally match each other. The studied nanocomposite is schematically visualized in Figure 5a. Fe_3Al was modeled by a 16-atom conventional cell depicted in the upper part of in Figure 5a. The α -phase represents a challenge for quantum-mechanical calculations because it lacks any long-range periodicity. We used a 16-atom supercell with atoms distributed according to so-called special quasi-random structure (SQS) concept.

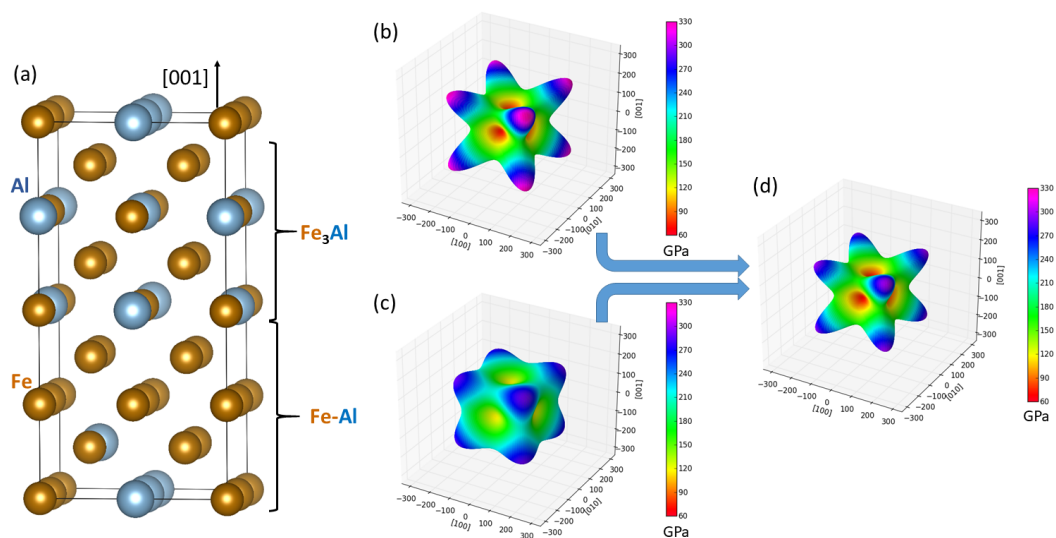


Figure 5. Visualization of a $\text{Fe}_3\text{Al}/\text{Fe-Al}$ nanocomposite (a superlattice) with the stacking along (and the interfaces perpendicular to) the $[001]$ direction (a) accompanied with directional dependences of the Young's modulus of bulk Fe_3Al (b), bulk Fe-Al (c) and the nanocomposite $\text{Fe}_3\text{Al}/\text{Fe-Al}$ (d) formed out of them. Parts (b–d) were visualized by the SC-EMA [79–81] library (scema.mpie.de) based on ab initio computed elastic constants.

The nanocomposite was formed by stacking the Fe_3Al on top of the α -phase along the $[001]$ direction (the interfaces are perpendicular to this direction). In contrast to the above-discussed cases of

superlattices formed by pairs of ordered transition-metal disilicides, when the both interfaces in the simulation supercell were identical, the supercells modeling the Fe-Al-based nanocomposites have different interfaces due to different distribution of atoms in the disordered α -phase. The interface energies were then averaged values related to the two interfaces. As another difference between the pairs of structurally and elastically nearly identical disilicides discussed above, the two constituting phases have clearly distinguishable elastic properties. Again, they are conveniently visualized in the form of directional dependences of the Young's modulus in Figure 5b,c for the Fe₃Al and the Fe-Al α -phase, respectively. The calculated values of elastic constants for Fe₃Al compound are $C_{11} = 211$ GPa, $C_{12} = 161$ GPa and $C_{44} = 139$ GPa. The elastic constants calculated for the disordered Fe-Al α -phase were projected onto a set of elastic constants possessing a cubic symmetry according to the rigorous mathematical theory by Moakher and Norris [87]. Similar concepts are often used in case of systems with any form of disorder (see, e.g., Refs. [59,88–91]). The resulting cubic-symmetry elastic constants are $C_{11} = 217$ GPa, $C_{12} = 131$ GPa and $C_{44} = 120$ GPa. Both phases exhibit $\langle 001 \rangle$ directions as elastically soft and $\langle 111 \rangle$ directions as elastically hard (i.e., with the minimum and maximum values of the Young's modulus, respectively). The Fe₃Al is also apparently elastically more anisotropic. The overall elasticity of their composite is then shown in Figure 5d.

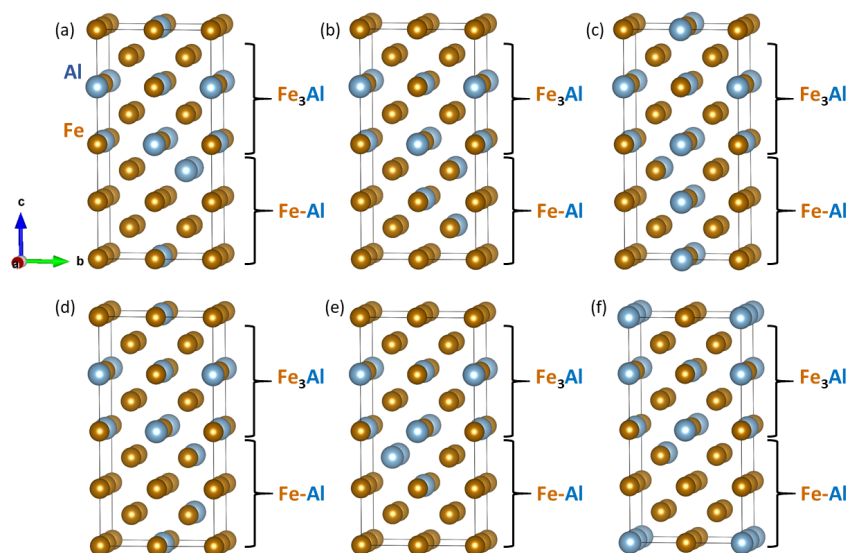


Figure 6. Schematic visualizations of different computed Fe₃Al/Fe-Al nanocomposites. The computed variants shown in sub-figures (a–f) differ by the distribution of atoms in the disordered Fe-Al phase.

Importantly, the interface energy was found to be ultra low again, only 0.005 J/m², which represents an energy difference appearing in Equation ((1)) smaller than 0.001 eV/atom, i.e., within the error-bar of our calculations. To determine an impact of distribution of atoms in the disordered Fe-Al α -phase on the interface energies, we performed a series of six additional calculations for supercells which have the same stoichiometry but differ in distributions of atoms in the Fe-Al α -phase (see Figure 6). In fact, the structure of coordination shells of atoms remain the same. For example, considering the Al atoms, their distribution in the part corresponding to the Fe-Al α -phase in the structural variants in Figure 6 are the same but the part of the supercell corresponding to the Fe-Al α -phase is either rotated and/or the atomic planes are permuted. As far as the latter process is concerned, if the atomic planes perpendicular to the $[001]$ direction in the α -phase part of Figure 5a would be numbered 1, 2, 3, 4, then by a permutation is meant, e.g., an arrangement 2, 3, 4, 1. Importantly, if being in a single-phase bulk, such permutation of atomic planes within the periodically repeated cell or rotations of the whole cell would not change the energy because the position of the origin

of coordinates (and the attached coordinate frame) can be arbitrarily shifted with respect to the crystal lattice.

Table 3. Calculated elastic constants of Fe₃Al/Fe-Al nanocomposites with the stacking along (and the interfaces perpendicular to) the [001] direction. The nanocomposites are visualized in Figure 6.

Variant	C ₁₁ (GPa)	C ₁₂ (GPa)	C ₁₃ (GPa)	C ₂₂ (GPa)	C ₂₃ (GPa)	C ₃₃ (GPa)	C ₄₄ (GPa)	C ₅₅ (GPa)	C ₆₆ (GPa)
Fe ₃ Al/Fe-Al Figure 6a	188	143	134	201	139	199	120	126	124
Fe ₃ Al/Fe-Al Figure 6b	186	134	142	185	141	199	123	123	123
Fe ₃ Al/Fe-Al Figure 6c	197	146	145	196	145	184	129	129	124
Fe ₃ Al/Fe-Al Figure 6d	200	151	143	199	143	200	125	125	122
Fe ₃ Al/Fe-Al Figure 6e	183	135	138	189	136	202	117	124	123
Fe ₃ Al/Fe-Al Figure 6f	175	141	137	189	145	200	121	126	127

The situation is, on the other hand, different in nanocomposites because the interface represents a reference point not existing in the single-phase bulk. The calculated energies are covering a broader range: 0.055 J/m² (Figure 6a), 0.021 J/m² (Figure 6b), 0.032 J/m² (Figure 6c), 0.006 J/m² (Figure 6d), 0.139 J/m² (Figure 6e), and 0.014 J/m² (Figure 6f). While this sensitivity on the atomic distribution is rather significant, the elastic properties of nanocomposites shown in Figure 6 are very similar. The computed values of elastic constants are summarized in Table 3.

As both phases appearing in the studied nanocomposites are magnetic, we further examined local magnetic moments of the iron atoms in configurations visualized in Figure 6a–f. The magnitude of local magnetic moments are shown in Figure 7 by the diameter of the spheres representing the Fe atoms. The lowest and the highest value (1.8 μ_B and 2.44 μ_B) are explicitly mentioned in Figure 7a to demonstrate a scaling, by which the magnitude of the local magnetic moment is indicated by the diameter of the spheres. Importantly, the magnetic properties of the Fe atoms turned out to be very sensitive to the distribution of atoms (they are reduced when the Al atoms are nearby).

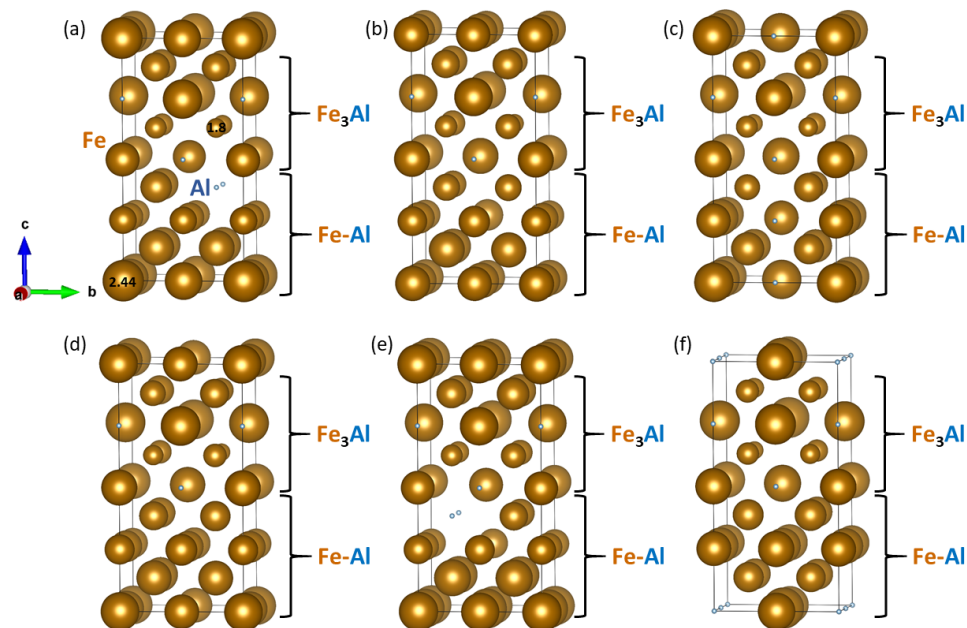


Figure 7. Calculated local magnetic moments of iron atoms (the magnitude is indicated by the diameter of the spheres representing the Fe atoms). The local magnetic moments shown in sub-figures (a–f) correspond to atomic distributions of nanocomposites visualized in sub-figures (a–f) of Figure 6, respectively.

4. Discussion

The above-discussed ultra low interface energies in the $\text{MoSi}_2/\text{WSi}_2$ nanocomposites may also indicate that both constituents are prone to mixing even at the atomic level. Indeed, it seems that longer annealing times lead to formation of solid-solution phases rather than (nano)composites. For example, $\text{MoSi}_2/\text{WSi}_2$ powders are synthesized by means of self-propagating high temperature combustion in [92] but solid solutions of $\text{MoSi}_2/\text{WSi}_2$ and $\text{Mo}_5\text{Si}_3/\text{W}_5\text{Si}_3$ are found. In [93], it is also reported that it is hard to distinguish MoSi_2 and WSi_2 phases and $(\text{W},\text{Mo})\text{Si}_2$ mainly in solid solution is found in Ref. [94]. The difficulties to distinguish MoSi_2 and WSi_2 Bragg peaks can be attributed to tetragonal MoSi_2 and WSi_2 phase having a long-range structure with very similar lattice constants (a is equal to 0.3202 nm and 0.3211, c amounts to 0.7855nm and 0.7835nm, respectively) [83]. It is also confirmed that $\text{MoSi}_2/\text{WSi}_2$ solid solution powder with nanometric $(\text{Mo},\text{W})\text{Si}_2$ structure forms via combustion synthesis method from the mechanical activated powder mixture [95].

To test the scenario of a random solid solution of Mo and W within a C11_b lattice, we performed a series of calculations for supercells modeling these states (see Figure 8a–d). The corresponding enthalpies of mixing (evaluated with respect to the energy of MoSi_2 and WSi_2 as reference end-members) are shown in Figure 8e and all of them are between zero and -0.001 eV/atom, i.e., within the error-bar of our calculations and comparable to the energy differences obtained when simulating the $\text{MoSi}_2/\text{WSi}_2$ nanocomposites.

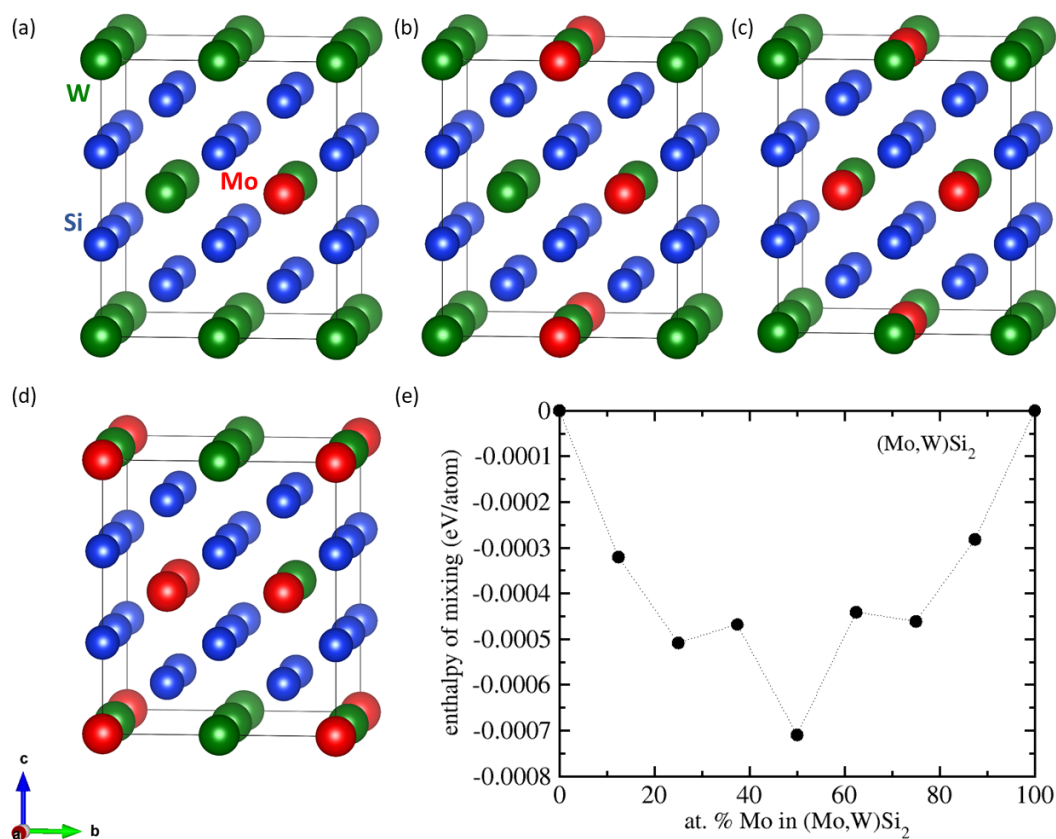


Figure 8. Schematic visualization of the supercells modeling random solid solutions of Mo and W within a C11_b lattice in the case of Mo:W ratio equal to 1:7 (a), 2:6 (b), 3:5 (c), and 4:4 (d) together with the corresponding enthalpies of mixing (e). The supercells for the Mo:W ratios equal to 5:3, 6:2 and 7:1 were obtained by swapping Mo and W atoms in the supercells shown in sub-figures (a–c). The atoms in the 32-atom supercells ($2 \times 2 \times 1$ multiple of 6-atom conventional cell of the C11_b structure) were distributed according to the special quasi-random structure (SQS) concept [96].

The above-discussed competition between formation of two-phase nanocomposites on the one hand and single-phase solid solutions on the other hand probably explains why a suitable preparation route is still being searched for in the case of TaSi₂/NbSi₂ nanocomposites when Nb solubility in TaSi₂ extremely large [97]. Our results related to the TaSi₂/NbSi₂ nanocomposites are intended as a motivation for future studies of this interesting system.

5. Conclusions

We performed a first-principles study of structural, thermodynamic and elastic properties of nanocomposites exhibiting ultra low or low interface energies. As examples of systems with predominantly covalent interatomic bonds, we studied two combinations of transition-metal disilicides: (i) MoSi₂/WSi₂ nanocomposites with individual constituents crystallizing in the tetragonal C11_b structure; and (ii) TaSi₂/NbSi₂ with the two components crystallizing in the hexagonal C40 structure. The constituents within each pair of materials exhibit very similar structural and elastic properties and we obtained ultra low (nearly zero) interface energy for their nanocomposites (within the error bar of our calculations, i.e., about 0.005 J/m²). The interface energy was found to be nearly independent on the width of individual constituents within the nanocomposites and/or crystallographic orientation of the interfaces.

As an example of a magnetic system, a pair of metallic phases containing from the Fe-Al system with different atomic ordering was considered. In particular, we simulated coherent superlattices formed by an ordered Fe₃Al intermetallic compound and a disordered Fe-Al phase with 18.75 at.% Al, the α -phase. Both constituents are structurally and elastically rather similar (but less than the two pairs of studied disilicides). To estimate the interface energy in the nanocomposite containing the disordered α -phase, which lacks a long-range periodicity, we simulated seven different distributions of atoms in the α -phase interfacing the Fe₃Al intermetallic compound. The resulting interface energies were again either ultra low or low, from 0.005 to 0.139 J/m². While the impact of atomic distribution on the elastic properties was found insignificant, the local magnetic moments of the iron atoms sensitively depended on the type and the distribution of surrounding atoms.

Author Contributions: Conceptualization, M.F.; Methodology, D.H.; Resources, M.Š. and M.F.; Writing—Original Draft Preparation, M.F.; Writing—Review and Editing, D.H. and M.Š.; Visualization, M.F.; Supervision, M.Š.; Project Administration, M.Š. and M.F.; and Funding Acquisition, M.Š. and M.F.

Funding: The authors acknowledge the Czech Science Foundation for the financial support received under the Project Nos. 16-24711S (M.Š.) and 17-22139S (M.F.). Additional resources were provided by the Academy of Sciences of the Czech Republic through the Fellowship of J. E. Purkyně (M.F.) and by the Ministry of Education, Youth and Sports of the Czech Republic under the Project CEITEC 2020, LQ1601 (M.Š.). D.H. acknowledges financial support from the Austrian Science Fund (FWF), Project Number P30341-N36. The computational results presented have been achieved in part using the Vienna Scientific Cluster (VSC).

Acknowledgments: M.F. and M.Š. acknowledge the support from the Academy of Sciences of the Czech Republic (Institutional Project No. RVO:68081723) and from the Ministry of Education, Youth and Sports of the Czech Republic via the research infrastructure IPMINFRA, LM2015069. Computational resources were made available by the Ministry of Education, Youth and Sports of the Czech Republic under the Projects CESNET (Project No. LM2015042), CERIT-Scientific Cloud (Project No. LM2015085) and IT4Innovations National Supercomputer Center (Project No. LM2015070) within the program Projects of Large Research, Development and Innovations Infrastructures. Figures 1a, 2, 3a, 4, 5a, 6, 8a–d, and A1a,b were visualized using the VESTA package [98].

Conflicts of Interest: The authors declare no conflict of interest.

Appendix A

To analyze the dependence of the ultra-low interface energies in the MoSi₂/WSi₂ nanocomposites on the crystallographic orientation of the interface, we computed properties of two other superlattices with the interfaces perpendicular to the [010] and [110] directions, respectively. The corresponding supercells modeling these nanocomposites are shown in Figure A1a,b, respectively. The elastic properties of these superlattices are visualized in the form of directional dependences of the Young's

modulus in Figure A1c,d. It is obvious that they are again very similar to each other and also very similar to that of the superlattice with the interfaces perpendicular to the [001] direction.

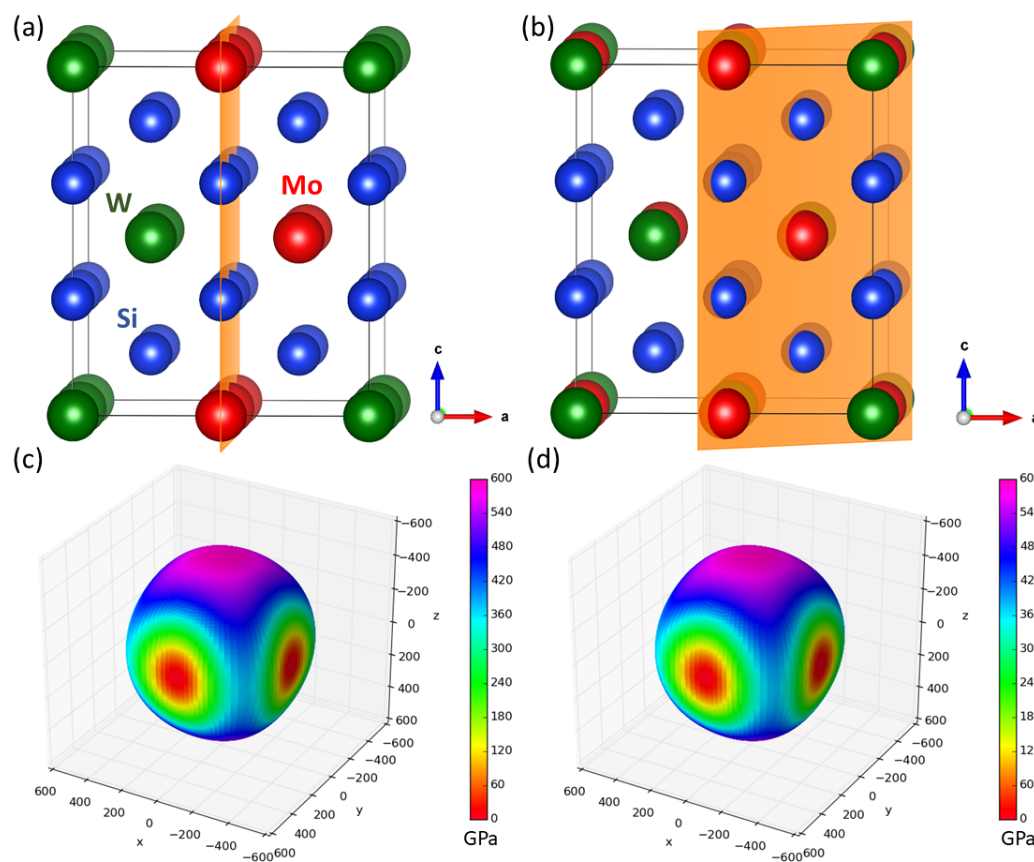


Figure A1. Schematics of computational supercells of MoSi₂/WSi₂ nanocomposites (superlattices) with the stacking along (and the interfaces perpendicular to) the [010] (a) and [110] (b) directions within the C11_b lattice, respectively. The interface planes are marked by orange color. The calculated elastic constants for these superlattices are shown as directional dependences of the Young's modulus for the composite with the [010] stacking direction (c) as well as that with the [110] stacking direction (d). Parts (c,d) were visualized by the SC-EMA [79–81] library (scema.mpie.de) based on *ab initio* computed elastic constants.

References

1. Yamaguchi, M.; Inui, H.; Ito, K. High-temperature structural intermetallics. *Acta Mater.* **2000**, *48*, 307–322. [[CrossRef](#)]
2. Umakoshi, Y.; Nakano, T.; Kishimoto, K.; Furuta, D.; Hagihara, K.; Azuma, M. Strength and deformation mechanism of C40-based single crystal and polycrystalline silicides. *Mater. Sci. Eng. A* **1999**, *261*, 113–121. [[CrossRef](#)]
3. Petrovic, J.; Vasudevan, A. Key developments in high temperature structural silicides. *Mater. Sci. Eng. A* **1999**, *261*, 1–5. [[CrossRef](#)]
4. Inui, H.; Moriwaki, M.; Yamaguchi, M. Plastic deformation of single crystals of VSi₂ and TaSi₂ with the C40 structure. *Intermetallics* **1998**, *6*, 723–728. [[CrossRef](#)]
5. Zhou, Y.; Zhang, Z.; Jin, X.; Ye, G.; Liu, C. Fabrication and Composition Investigation of WSi₂/MoSi₂ Composite Powders Obtained by a Self-Propagating High-Temperature Synthesis Method. *Arabian J. Sci. Eng.* **2016**, *41*, 2583–2587. [[CrossRef](#)]
6. Deevi, S.C. Self-propagating high-temperature synthesis of molybdenum disilicide. *J. Mater. Sci.* **1991**, *26*, 3343–3353. [[CrossRef](#)]

7. Ke, P.; Yi, M.; Ran, L. Reaction thermodynamics of MoSi₂-WSi₂ composites in the thermal explosion mode of SHS. *Rare Met. Mater. Eng.* **2006**, *35*, 554–558.
8. Zhang, H.; Chen, P.; Wang, M.; Liu, X. Room-temperature mechanical properties of WSi₂/MoSi₂ composites. *Rare Met.* **2002**, *21*, 304–307.
9. Chen, F.; Xu, J.; Liu, Y.; Cai, L. In situ reactive spark plasma sintering of WSi₂/MoSi₂ composites. *Ceram. Int.* **2016**, *42*, 11165–11169. [[CrossRef](#)]
10. Zamani, S.; Bakhsheshi-Rad, H.R.; Kadir, M.R.A.; Shafiee, M.R.M. Synthesis and kinetic study of (Mo,W)Si₂-WSi₂ nanocomposite by mechanical alloying. *J. Alloys Compd.* **2012**, *540*, 248–259. [[CrossRef](#)]
11. Xu, J.; Wang, Y.; Weng, B.; Chen, F. Preparation and Characterization of MoSi₂/WSi₂ Composites from MASHSed Powder. *Mater. Trans.* **2015**, *56*, 313–316. [[CrossRef](#)]
12. Kattner, U.; Burton, B. Al-Fe (Aluminium-Iron). In *Phase Diagrams of Binary Iron Alloys*; Okamoto, H., Ed.; ASM International: Materials Park, OH, USA, 1993; pp. 12–28.
13. Sauthoff, G. *Intermetallics*; VCH Verlagsgesellschaft: Weinheim, Germany, 1995.
14. Liu, C.T.; Stringer, J.; Mundy, J.N.; Horton, L.L.; Angelini, P. Ordered intermetallic alloys: An assessment. *Intermetallics* **1997**, *5*, 579–596. [[CrossRef](#)]
15. Stoloff, N.S. Iron aluminides: Present status and future prospects. *Mater. Sci. Eng. A* **1998**, *258*, 1–14. [[CrossRef](#)]
16. Palm, M.; Inden, G.; Thomas, N. The Fe-Al-Ti system. *J. Phase Equilib.* **1995**, *16*, 209–222. [[CrossRef](#)]
17. Palm, M.; Lacaze, J. Assessment of the Al-Fe-Ti system. *Intermetallics* **2006**, *14*, 1291–1303. [[CrossRef](#)]
18. Palm, M.; Sauthoff, G. Deformation behaviour and oxidation resistance of single-phase and two-phase L₂₁-ordered Fe-Al-Ti alloys. *Intermetallics* **2004**, *12*, 1345–1359. [[CrossRef](#)]
19. Sundman, B.; Ohnuma, I.; Dupin, N.; Kattner, U.R.; Fries, S.G. An assessment of the entire Al-Fe system including D0(3) ordering. *Acta Mater.* **2009**, *57*, 2896–2908. [[CrossRef](#)]
20. Stein, F.; Palm, M. Re-determination of transition temperatures in the Fe-Al system by differential thermal analysis. *Int. J. Mater. Res.* **2007**, *98*, 580–588. [[CrossRef](#)]
21. Palm, M. Fe-Al materials for structural applications at high temperatures: Current research at MPIE. *Int. J. Mater. Res.* **2009**, *100*, 277–287. [[CrossRef](#)]
22. Watson, R.E.; Weinert, M. Transition-metal aluminide formation: Ti, V, Fe, and Ni aluminides. *Phys. Rev. B* **1998**, *58*, 5981–5988. [[CrossRef](#)]
23. Gonzales-Ormeno, P.; Petrilli, H.; Schon, C. Ab-initio calculations of the formation energies of BCC-based superlattices in the Fe-Al system. *Calphad* **2002**, *26*, 573. [[CrossRef](#)]
24. Friák, M.; Neugebauer, J. Ab initio study of the anomalous volume-composition dependence in Fe-Al alloys. *Intermetallics* **2010**, *18*, 1316–1321. [[CrossRef](#)]
25. Amara, H.; Fu, C.C.; Soisson, F.; Maugis, P. Aluminum and vacancies in α -iron: Dissolution, diffusion, and clustering. *Phys. Rev. B* **2010**, *81*, 174101. [[CrossRef](#)]
26. Liu, S.; Duan, S.; Ma, B. First-principles calculation of vibrational entropy for Fe-Al compounds. *Phys. Rev. B* **1998**, *58*, 9705–9709.
27. Kulikov, N.I.; Postnikov, A.V.; Borstel, G.; Braun, J. Onset of magnetism in B2 transition-metal aluminides. *Phys. Rev. B* **1999**, *59*, 6824–6833. [[CrossRef](#)]
28. Fähnle, M.; Drautz, R.; Lechermann, F.; Singer, R.; Diaz-Ortiz, A.; Dosch, H. Thermodynamic properties from ab-initio calculations: New theoretical developments, and applications to various materials systems. *Phys. Status Solidi B-Basic Solid State Phys.* **2005**, *242*, 1159–1173. [[CrossRef](#)]
29. Friák, M.; Deges, J.; Krein, R.; Frommeyer, G.; Neugebauer, J. Combined ab initio and experimental study of structural and elastic properties of Fe₃Al-based ternaries. *Intermetallics* **2010**, *18*, 1310. [[CrossRef](#)]
30. Kirklin, S.; Saal, J.E.; Hegde, V.I.; Wolverton, C. High-throughput computational search for strengthening precipitates in alloys. *Acta Mater.* **2016**, *102*, 125–135. [[CrossRef](#)]
31. Airiskallio, E.; Nurmi, E.; Heinonen, M.H.; Vayrynen, I.J.; Kokko, K.; Ropo, M.; Punkkinen, M.P.J.; Pitkanen, H.; Alatalo, M.; Kollar, J.; Johansson, B.; Vitos, L. High temperature oxidation of Fe-Al and Fe-Cr-Al alloys: The role of Cr as a chemically active element. *Corros. Sci.* **2010**, *52*, 3394–3404. [[CrossRef](#)]
32. Medvedeva, N.I.; Park, M.S.; Van Aken, D.C.; Medvedeva, J.E. First-principles study of Mn, Al and C distribution and their effect on stacking fault energies in fcc Fe. *J. Alloy. Compd.* **2014**, *582*, 475–482. [[CrossRef](#)]
33. Čížek, J.; Lukáč, F.; Procházka, I.; Kužel, R.; Jirásková, Y.; Janičkovič, D.; Anwand, W.; Brauer, G. Characterization of quenched-in vacancies in Fe-Al alloys. *Physica B* **2012**, *407*, 2659–2664. [[CrossRef](#)]

34. Ipsier, H.; Semenova, O.; Krachler, R. Intermetallic phases with DO_3 -structure: A statistical-thermodynamic model. *J. Alloy. Compd.* **2002**, *338*, 20–25. [[CrossRef](#)]
35. Miháliková, I.; Slávik, A.; Friák, M.; Všianská, M.; Koutrná, N.; Holec, D.; Šob, M. First-principles study of interface energies in Fe-Al-based superalloy nanocomposites. In *NANOCON 2017 Conference Proceedings (9th International Conference on Nanomaterials—Research & Application, Brno, Oct. 18–20, 2017)*; Tanger Ltd.: Ostrava, Czech Republic; 2017; pp. 69–74.
36. Šesták, P.; Friák, M.; Holec, D.; Všianská, M.; Šob, M. Strength and Brittleness of Interfaces in Fe-Al Superalloy Nanocomposites under Multiaxial Loading: An ab initio and Atomistic Study. *Nanomaterials* **2018**, *8*, 873. [[CrossRef](#)] [[PubMed](#)]
37. Lechermann, F.; Welsch, F.; Elsässer, C.; Ederer, C.; Fähnle, M.; Sanchez, J.; Meyer, B. Density-functional study of Fe_3Al : LSDA versus GGA. *Phys. Rev. B* **2002**, *65*, 132104. [[CrossRef](#)]
38. Connetable, D.; Maugis, P. First principle calculations of the kappa- Fe_3AlC perovskite and iron-aluminium intermetallics. *Intermetallics* **2008**, *16*, 345–352. [[CrossRef](#)]
39. Lechermann, F.; Fähnle, M.; Meyer, B.; Elsässer, C. Electronic correlations, magnetism, and structure of Fe-Al subsystems: An LDA+U study. *Phys. Rev. B* **2004**, *69*, 165116. [[CrossRef](#)]
40. Kellou, A.; Grosdidier, T.; Raulot, J.M.; Aourag, H. Atomistic study of magnetism effect on structural stability in Fe_3Al and Fe_3AlX ($X = H, B, C, N, O$) alloys. *Phys. Status Solidi B-Basic Solid State Phys.* **2008**, *245*, 750–755. [[CrossRef](#)]
41. Jiraskova, Y.; Pizurova, N.; Titov, A.; Janickovic, D.; Friak, M. Phase separation in Fe-Ti-Al alloy—Structural, magnetic, and Moessbauer study. *J. Magn. Magn. Mater.* **2018**, *468*, 91–99. [[CrossRef](#)]
42. Wang, K.; Wang, Y.; Cheng, Y. The Formation and Dynamic Evolution of Antiphase Domain Boundary in FeAl Alloy: Computational Simulation in Atomic Scale. *Mater. Res. Ibero-Am. J. Mater.* **2018**, *21*, e20171048. [[CrossRef](#)]
43. Balagurov, A.M.; Bobrikov, I.A.; Sumnikov, V.S.; Golovin, I.S. Antiphase domains or dispersed clusters? Neutron diffraction study of coherent atomic ordering in Fe_3Al -type alloys. *Acta Mater.* **2018**, *153*, 45–52. [[CrossRef](#)]
44. Murakami, Y.; Niitsu, K.; Tanigaki, T.; Kainuma, R.; Park, H.S.; Shindo, D. Magnetization amplified by structural disorder within nanometre-scale interface region. *Nat. Commun.* **2014**, *5*, 4133. [[CrossRef](#)] [[PubMed](#)]
45. Oguma, R.; Matsumura, S.; Eguchi, T. Kinetics of B2-and DO_3 type ordering and formation of domain structures in Fe-Al alloys. *J. Phys. Cond. Matter* **2008**, *20*, 275225. [[CrossRef](#)] [[PubMed](#)]
46. Hohenberg, P.; Kohn, W. Inhomogeneous electron gas. *Phys. Rev.* **1964**, *136*, B864–B871. [[CrossRef](#)]
47. Kohn, W.; Sham, L.J. Self-consistent equations including exchange and correlation effects. *Phys. Rev.* **1965**, *140*, A1133–A1138. [[CrossRef](#)]
48. Kresse, G.; Hafner, J. Ab initio molecular dynamics for liquid metals. *Phys. Rev. B* **1993**, *47*, 558–561. [[CrossRef](#)]
49. Kresse, G.; Furthmüller, J. Efficient iterative schemes for ab initio total-energy calculations using a plane-wave basis set. *Phys. Rev. B* **1996**, *54*, 11169–11186. [[CrossRef](#)]
50. Blöchl, P.E. Projector augmented-wave method. *Phys. Rev. B* **1994**, *50*, 17953–17979. [[CrossRef](#)]
51. Kresse, G.; Joubert, D. From ultrasoft pseudopotentials to the projector augmented-wave method. *Phys. Rev. B* **1999**, *59*, 1758. [[CrossRef](#)]
52. Ceperley, D.M.; Alder, B.J. Ground State of the Electron Gas by a Stochastic Method. *Phys. Rev. Lett.* **1980**, *45*, 566–569. [[CrossRef](#)]
53. Perdew, J.P.; Wang, Y. Accurate and simple analytic representation of the electron-gas correlation energy. *Phys. Rev. B* **1992**, *45*, 13244–13249. [[CrossRef](#)]
54. Vosko, S.H.; Wilk, L.; Nusair, M. Accurate spin-dependent electron liquid correlation energies for local spin density calculations: A critical analysis. *Can. J. Phys.* **1980**, *58*, 1200. [[CrossRef](#)]
55. Monkhorst, H.J.; Pack, J.D. Special points for Brillouin-zone integrations. *Phys. Rev. B* **1976**, *13*, 5188–5192. [[CrossRef](#)]
56. Zhou, L.; Holec, D.; Mayrhofer, P.H. First-principles study of elastic properties of Cr-Al-N. *J. Appl. Phys.* **2013**, *113*, 043511. [[CrossRef](#)]
57. Mayrhofer, P.H.; Fischer, F.D.; Boehm, H.J.; Mitterer, C.; Schneider, J.M. Energetic balance and kinetics for the decomposition of supersaturated $Ti_{1-x}Al_xN$. *Acta Mater.* **2007**, *55*, 1441–1446. [[CrossRef](#)]

58. Wu, L.; Chen, M.; Li, C.; Zhou, J.; Shen, L.; Wang, Y.; Zhong, Z.; Feng, M.; Zhang, Y.; Han, K.; et al. Ferromagnetism and matrix-dependent charge transfer in strained LaMnO₃-LaCoO₃ superlattices. *Mater. Res. Lett.* **2018**, *6*, 501–507. [[CrossRef](#)]
59. Koutná, N.; Holec, D.; Friák, M.; Mayrhofer, P.H.; Šob, M. Stability and elasticity of metastable solid solutions and superlattices in the MoN-TaN system: First-principles calculations. *Mater. Des.* **2018**, *144*, 310–322. [[CrossRef](#)]
60. Jiang, M.; Xiao, H.Y.; Peng, S.M.; Yang, G.X.; Liu, Z.J.; Zu, X.T. A comparative study of low energy radiation response of AlAs, GaAs and GaAs/AlAs superlattice and the damage effects on their electronic structures. *Sci. Rep.* **2018**, *8*, 2012. [[CrossRef](#)]
61. Wen, Y.N.; Gao, P.F.; Xia, M.G.; Zhang, S.L. Half-metallic ferromagnetism prediction in MoS₂-based two-dimensional superlattice from first-principles. *Mod. Phys. Lett. B* **2018**, *32*, 1850098. [[CrossRef](#)]
62. Friák, M.; Tytko, D.; Holec, D.; Choi, P.P.; Eisenlohr, P.; Raabe, D.; Neugebauer, J. Synergy of atom-probe structural data and quantum-mechanical calculations in a theory-guided design of extreme-stiffness superlattices containing metastable phases. *New J. Phys.* **2015**, *17*, 093004. [[CrossRef](#)]
63. Dai, Q.; Eckern, U.; Schwingenschlog, U. Effects of oxygen vacancies on the electronic structure of the (LaVO₃)₆/SrVO₃ superlattice: A computational study. *New J. Phys.* **2018**, *20*, 073011. [[CrossRef](#)]
64. Jiang, M.; Xiao, H.; Peng, S.; Qiao, L.; Yang, G.; Liu, Z.; Zu, X. First-Principles Study of Point Defects in GaAs/AlAs Superlattice: the Phase Stability and the Effects on the Band Structure and Carrier Mobility. *Nanoscale Res. Lett.* **2018**, *13*, 301. [[CrossRef](#)]
65. Chen, H.; Millis, A.J.; Marianetti, C.A. Engineering Correlation Effects via Artificially Designed Oxide Superlattices. *Phys. Rev. Lett.* **2013**, *111*, 116403. [[CrossRef](#)] [[PubMed](#)]
66. Mottura, A.; Janotti, A.; Pollock, T.M. A first-principles study of the effect of Ta on the superlattice intrinsic stacking fault energy of L1₂-Co₃(Al,W). *Intermetallics* **2012**, *28*, 138–143. [[CrossRef](#)]
67. Rosenggaard, N.; Skriver, H. Ab-initio study of antiphase boundaries and stacking-faults in L1₂ and D0₂₂ compounds. *Phys. Rev. B* **1994**, *50*, 4848–4858. [[CrossRef](#)]
68. Torres-Pardo, A.; Gloter, A.; Zubko, P.; Jecklin, N.; Lichtensteiger, C.; Colliex, C.; Triscone, J.M.; Stephan, O. Spectroscopic mapping of local structural distortions in ferroelectric PbTiO₃/SrTiO₃ superlattices at the unit-cell scale. *Phys. Rev. B* **2011**, *84*, 220102. [[CrossRef](#)]
69. Chawla, V.; Holec, D.; Mayrhofer, P.H. Stabilization criteria for cubic AlN in TiN/AlN and CrN/AlN bi-layer systems. *J. Phys. D* **2013**, *46*, 045305. [[CrossRef](#)]
70. Cooper, V.R.; Rabe, K.M. Enhancing piezoelectricity through polarization-strain coupling in ferroelectric superlattices. *Phys. Rev. B* **2009**, *79*, 180101. [[CrossRef](#)]
71. Chen, B.; Zhang, Q.; Bernholc, J. Si diffusion in GaAs and Si-induced interdiffusion in GaAs/AlAs superlattices. *Phys. Rev. B* **1994**, *49*, 2985–2988. [[CrossRef](#)]
72. Schmid, U.; Christensen, N.; Cardona, M.; Lukes, F.; Ploog, K. Optical anisotropy in GaAs/AlS(110) superlattices. *Phys. Rev. B* **1992**, *45*, 3546–3551. [[CrossRef](#)]
73. Gibson, Q.D.; Schoop, L.M.; Weber, A.P.; Ji, H.; Nadj-Perge, S.; Drozdov, I.K.; Beidenkopf, H.; Sadowski, J.T.; Fedorov, A.; Yazdani, A.; Valla, T.; Cava, R.J. Termination-dependent topological surface states of the natural superlattice phase Bi₄Se₃. *Phys. Rev. B* **2013**, *88*, 081108R. [[CrossRef](#)]
74. Park, C.; Chang, K. Structural and electronic-properties of GaP-AlP (001) superlattices. *Phys. Rev. B* **1993**, *47*, 12709–12715. [[CrossRef](#)]
75. Romanyuk, O.; Hannappel, T.; Grosse, F. Atomic and electronic structure of GaP/Si(111), GaP/Si(110), and GaP/Si(113) interfaces and superlattices studied by density functional theory. *Phys. Rev. B* **2013**, *88*, 115312. [[CrossRef](#)]
76. Abdulsattar, M.A. SiGe superlattice nanocrystal pure and doped with substitutional phosphorus single atom: Density functional theory study. *Superlattices Microstruct.* **2011**, *50*, 377–385. [[CrossRef](#)]
77. Botti, S.; Vast, N.; Reining, L.; Olevano, V.; Andreani, L. Ab initio and semiempirical dielectric response of superlattices. *Phys. Rev. B* **2004**, *70*, 045301. [[CrossRef](#)]
78. Rondinelli, J.M.; Spaldin, N.A. Electron-lattice instabilities suppress cuprate-like electronic structures in SrFeO₃/OSrTiO₃ superlattices. *Phys. Rev. B* **2010**, *81*, 085109. [[CrossRef](#)]
79. Titrián, H.; Aydin, U.; Friák, M.; Ma, D.; Raabe, D.; Neugebauer, J. Self-consistent Scale-bridging Approach to Compute the Elasticity of Multi-phase Polycrystalline Materials. *MRS Proc.* **2013**, *1524*, rr06. [[CrossRef](#)]

80. Friák, M.; Counts, W.; Ma, D.; Sander, B.; Holec, D.; Raabe, D.; Neugebauer, J. Theory-Guided Materials Design of Multi-Phase Ti-Nb Alloys with Bone-Matching Elastic Properties. *Materials* **2012**, *5*, 1853–1872. [[CrossRef](#)]
81. Zhu, L.F.; Friák, M.; Lymperakis, L.; Titrian, H.; Aydin, U.; Janus, A.; Fabritius, H.O.; Ziegler, A.; Nikolov, S.; Hemzalová, P.; Raabe, D.; Neugebauer, J. Ab initio study of single-crystalline and polycrystalline elastic properties of Mg-substituted calcite crystals. *J. Mech. Behav. Biomed. Mater.* **2013**, *20*, 296–304. [[CrossRef](#)]
82. Nakamura, M.; Matsumoto, S.; Hirano, T. Elastic constants of MoSi₂ and WSi₂ single crystals. *J. Mater. Sci.* **1990**, *25*, 3309–3313. [[CrossRef](#)]
83. Zhang, H.; Chen, P.; Yan, J.; Tang, S. Fabrication and wear characteristics of MoSi₂ matrix composite reinforced by WSi₂ and La₂O₃. *Int. J. Refract. Met. Hard Mater.* **2004**, *22*, 271–275. [[CrossRef](#)]
84. Chu, F.; Ming, L.; Maloy, S.A.; Mitchell, T.E.; Migliori, A.; Garrett, J. Single crystal elastic constants of NbSi₂. *Philos. Mag. B* **1995**, *71*, 373–382. [[CrossRef](#)]
85. Erturk, E.; Gurel, T. Ab initio study of structural, elastic, and vibrational properties of transition-metal disilicides NbSi₂ and TaSi₂ in hexagonal C40 structure. *Phys. B Cond. Matter* **2018**, *537*, 188–193. [[CrossRef](#)]
86. Wan, B.; Xiao, F.; Zhang, Y.; Zhao, Y.; Wu, L.; Zhang, J.; Gou, H. Theoretical study of structural characteristics, mechanical properties and electronic structure of metal (TM=V, Nb and Ta) silicides. *J. Alloys Compd.* **2016**, *681*, 412–420. [[CrossRef](#)]
87. Moakher, M.; Norris, A.N. The closest elastic tensor of arbitrary symmetry to an elasticity tensor of lower symmetry. *J. Elast.* **2006**, *85*, 215–263. [[CrossRef](#)]
88. Tasnádi, F.; Abrikosov, I.A.; Rogström, L.; Almer, J.; Johansson, M.P.; Oden, M. Significant elastic anisotropy in Ti_{1-x}Al_xN alloys. *Appl. Phys. Lett.* **2010**, *97*, 231902. [[CrossRef](#)]
89. Tasnádi, F.; Odén, M.; Abrikosov, I. Ab initio elastic tensor of cubic Ti_{0.5}Al_{0.5}N alloys: Dependence of elastic constants on size and shape of the supercell model and their convergence. *Phys. Rev. B* **2012**, *85*, 144112. [[CrossRef](#)]
90. Von Pezold, J.; Dick, A.; Friák, M.; Neugebauer, J. Generation and performance of special quasirandom structures for studying the elastic properties of random alloys: Application to Al-Ti. *Phys. Rev. B* **2010**, *81*, 094203. [[CrossRef](#)]
91. Holec, D.; Tasnádi, F.; Wagner, P.; Friák, M.; Neugebauer, J.; Mayrhofer, P.; Keckes, J. Macroscopic elastic properties of textured ZrN-AlN polycrystalline aggregates: From ab initio calculations to grainscale interactions. *Phys. Rev. B* **2014**, *90*, 184106. [[CrossRef](#)]
92. Kou, K.; Yang, Y.; Ai, Y.; Chen, Y.; Kang, M. Self-propagating high-temperature combustion synthesis of MoSi₂-WSi₂ composite. *Rare Met. Mater. Eng.* **2000**, *29*, 190–192.
93. Zhang, Y.; Zhang, P.; Ren, J.; Zhang, L.; Zhang, J. SiC nanowire-toughened MoSi₂-WSi₂-SiC-Si multiphase coating for improved oxidation resistance of C/C composites. *Ceram. Int.* **2016**, *42*, 12573–12580. [[CrossRef](#)]
94. Ai, Y.; Cheng, Y.; Yang, Y.; Kang, M.; Liu, C. Preparation and microstructure of WSi₂/MoSi₂ composite heat element. *Rare Met. Mater. Eng.* **2005**, *34*, 962–965.
95. Xu, J.; Wu, H.; Li, B. Synthesis of MoSi₂/WSi₂ nanocrystalline powder by mechanical-assistant combustion synthesis method. *Int. J. Refract. Met. Hard Mater.* **2010**, *28*, 217–220. [[CrossRef](#)]
96. Zunger, A.; Wei, S.; Ferreira, L.; Bernard, J. Special quasirandom structures. *Phys. Rev. Lett.* **1990**, *65*, 353–356. [[CrossRef](#)] [[PubMed](#)]
97. Li, J.; Wang, C.; Yao, J.; Yang, S.; Kang, Y.; Shi, Z.; Liu, X. Experimental investigation of phase equilibria in the Nb-Si-Ta ternary system. *Int. J. Mater. Res.* **2016**, *107*, 1112–1120. [[CrossRef](#)]
98. Momma, K.; Izumi, F. VESTA 3 for three-dimensional visualization of crystal, volumetric and morphology data. *J. Appl. Crystallogr.* **2011**, *44*, 1272–1276. [[CrossRef](#)]

